



# Linear and nonlinear optical response of sulfur-deficient nanocrystallite WS<sub>2</sub> thin films

Gobinda Pradhan<sup>1</sup> and Ashwini Kumar Sharma<sup>1,\*</sup>

<sup>1</sup>Department of Physics, Indian Institute of Technology Guwahati, Guwahati, Assam 781039, India

Received: 12 June 2019

Accepted: 31 August 2019

Published online:

9 September 2019

© Springer Science+Business Media, LLC, part of Springer Nature 2019

## ABSTRACT

Multilayered-to-bulk-like films were deposited by pulsed laser deposition at various argon gas deposition pressure where a significant amount of sulfur deficiency was observed. All films showed high atomic disorder and corresponding lattice distortion attributed to the large-scale sulfur deficiency. Instead of continuous film, huge sulfur deficiency created a mixed state of metallic tungsten and WS<sub>2</sub> nanocrystals of sizes 4–8 nm throughout the films. The as-deposited WS<sub>2</sub> films showed a dramatic shift in linear optical response, with the behavior resembling that of quantum dots. A significantly large reverse saturation absorption and positive nonlinear refraction response was observed in all the films, as measured by the open- and closed-aperture Z-scan experiment under He–Ne laser at 632.8 nm. In addition, third-order nonlinear optical susceptibility of the thin films was found to be of the order of 10<sup>-2</sup> esu as measured from Z-scan experiment. The anomalously high nonlinear optical response of the film was attributed to the continuous-wave laser-induced thermal nonlinearity dominance over optical nonlinearity. Optical limiting was also observed in the films where optical limiting thresholds were found to increase with an increase in nonlinear absorption coefficient.

## Introduction

In recent years, after graphene, a lot of attention has been devoted to the transition metal dichalcogenides (TMDCs) as a two-dimensional (2D) material due to their excellent electronic and optical properties and usefulness for optoelectronic devices [1–6]. Among all the TMDCs, significant progress has been made on molybdenum disulfide (MoS<sub>2</sub>), while the closely related tungsten disulfide (WS<sub>2</sub>), gaining attention only recently. WS<sub>2</sub> is emerging as a promising

alternative 2D material for new-generation electronics devices with its interesting thickness-dependent optical bandgap from visible [(2.1 eV (monolayer))] to infrared regions [1.3 eV (bulk)], high carrier mobility, high on–off switching ratio, and chemically stable and mechanically flexible structure [7–12].

Along with the processes like chemical vapor deposition, hydrothermal and sulfurization processes, and chemical and mechanical exfoliation, pulsed laser deposition (PLD) technique also shows its potential to synthesize mono-to-multilayered WS<sub>2</sub>

Address correspondence to E-mail: aksharma@iitg.ac.in

thin films [12–14]. In PLD, one can control film properties by optimizing various deposition parameters like ambient gas pressure, deposition temperature, laser wavelength and fluence, target-to-substrate distance, etc. [15–18]. Among the deposition parameters, ambient gas pressure during deposition plays a significant role in deposition rate, crystallinity, stoichiometry, and surface morphology of the deposited films [19, 20]. During deposition, oxygen and nitrogen gas atmosphere is used for oxide and nitride materials while inert gas (Ar, He) atmosphere or high vacuum is preferred for deposition of other reactive materials [20, 21]. In the last few years, WS<sub>2</sub> films of thicknesses monolayer to multilayer to a bulk-like structure have been deposited via PLD and their usefulness as photodetector, HER catalyst has been demonstrated in the literature [21–25]. Besides the interesting electrical and linear optical behavior, recently, notable optical nonlinearity has been also observed in monolayer to few-layered WS<sub>2</sub> films. Carlos et al. reported on the nonlinear optical properties of monolayer and few layers of WS<sub>2</sub> [26]. Zin et al. demonstrated a shift from saturable absorption to reverse saturable absorption of monolayer WS<sub>2</sub> with an increase in laser intensity [27]. In the present era, nonlinear optical materials are of great importance with their excellent modern applications like optical switcher, optical limiter, Q switcher, mode locker, harmonic generation, etc. [28–30]. Nowadays, various experimental techniques including degenerate four-wave mixing [31], nonlinear interferometry [32], Z-scan, ellipse rotation [33], etc., are used to determine nonlinear optical properties of materials. Among them, Z-scan technique is a simple and effective one [34]. Almost all the nonlinear optical parameters like nonlinear absorption (NLA) coefficient, nonlinear refractive index (NLR) coefficient, and nonlinear optical susceptibility can be easily obtained by Z-scan measurement. It is known that stoichiometry, crystallinity, and surface morphology of a thin film strongly affect the linear and nonlinear optical properties of the respective film. Hence, though optical nonlinearity in stoichiometric-layered WS<sub>2</sub> films has been reported, a systematic study on the nonlinear optical response of a nonstoichiometric, defect-induced ultrathin nanocrystallite WS<sub>2</sub> (nc-WS<sub>2</sub>) film is scarce.

In the present work, multilayered WS<sub>2</sub> films have been deposited by PLD at various argon (Ar) gas pressures. Variation in stoichiometry and

crystallinity of WS<sub>2</sub> film deposited at various Ar pressure and their corresponding effects on linear and nonlinear optical properties have been explored in detail. The layer structure and crystallinity of the films have been studied by Raman spectroscopy and XRD, while AFM and FESEM images are used to characterize the surface morphology. We further performed FETEM analysis of the films for better understanding of the nanostructures and crystallinity of the films. The linear optical properties of the WS<sub>2</sub> films are investigated with UV–Vis spectroscopy and spectroscopic ellipsometry, while the nonlinear optical properties are measured by Z-scan setup using He–Ne laser of wavelength 632.8 nm as the excitation source. Optical limiting is shown to be one of the possible applications in such films.

## Methods

WS<sub>2</sub> films were deposited by PLD technique at various Ar gas pressures. A second harmonic Q-switched Nd: YAG laser (Quanta-Ray INDI) of pulse width 8 ns and repetition rate 10 Hz (wavelength 532 nm) was used to ablate the solid WS<sub>2</sub> target (pellet) at a laser fluence of 2.2 J/cm<sup>2</sup>. The films were deposited onto Corning glass substrate heated to 400 °C under Ar gas atmosphere at a pressure of 10<sup>-1</sup>, 10<sup>-2</sup>, 10<sup>-3</sup> and 10<sup>-5</sup> mbar and the samples are designated as P<sub>1</sub>, P<sub>2</sub>, P<sub>3</sub>, and P<sub>4</sub>, respectively, for ease in presentation. All films were deposited for 6 min. The X-ray diffraction pattern (Rigaku, model TTRAX III) was recorded in the typical 2θ range from 5° to 70°. The samples were scanned at 3 °/min scanning speed with a step size of 0.03°. The X-ray source was Cu K<sub>α</sub> line (λ = 1.5406 Å). Raman characterization (Horiba Jobi Yvon, LabRam HR 800) of the films were carried out in the backscattering geometry. A laser source of wavelength of 488 nm was used for Raman mode excitation. The film thickness was measured using stylus profilometer (Veeco Dektak 150). The linear optical properties of the films were extracted with the help of spectroscopic ellipsometer (Semilab GES5-E).

The nonlinear optical behavior of the films was studied using Z-scan setup. A schematic diagram of the Z-scan setup is shown in Fig. 1. He–Ne laser (MELLES GRIOT 05-LHP-927) at a wavelength of 632.8 nm was used as the laser source which was focused onto the film surface using a bi-convex lens of focal length 5 cm. The film was placed on a

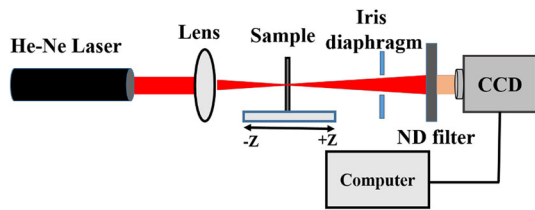
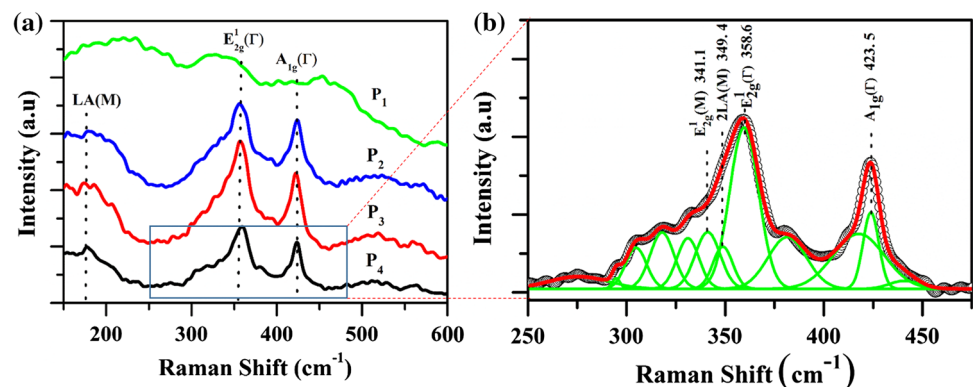


**Figure 1** Schematic diagram of Z-scan experimental setup.

translation stage which was translated on both sides (from  $-15$  to  $15$  mm with respect to the focused point of the lens) along the optical axis of the focused laser beam. The transmitted beam passing through the sample was recorded by a CCD camera (PCO PixelFly) connected with a computer. The transmitted laser beam through the film was recorded in every step of translation of the sample by  $1$  mm with respect to the focal plane. During experiment, a neutral density (ND) filter was set before CCD to avoid its saturation by high intensity laser beam. The unwanted scattered light was blocked from entering into CCD by placing an iris diaphragm before ND filter. The transmitted beam intensity is equivalent to the integrated gray values of recorded images as measured by the MATLAB programming. For the closed-aperture (CA) Z-scan, the images were extracted from full-size images (open aperture) by implementing an optimized size soft aperture using the MATLAB program. The aperture size was adjusted at certain value so that the ratio of integrated intensity of the image with aperture to that of full image was  $\sim 0.4$ . Thus, the Z-scan setup provides open as well as closed Z-scan data from a single recorded data only.

**Figure 2** Raman spectra of **a**  $\text{WS}_2$  films deposited at various argon gas pressures and **b** an enlarged view of deconvoluted Raman spectra of the  $P_4$  film in the range of  $250$ – $450$   $\text{cm}^{-1}$ .



## Results and discussion

Figure 2a shows the Raman spectra of the  $\text{WS}_2$  films deposited for 6 min at various Ar gas pressures. These spectra contain first-order Raman modes at the Brillouin zone center ( $E_{2g}^1(\Gamma)$  and  $A_{1g}(\Gamma)$ ). In addition to these two modes, the longitudinal acoustic mode at the M point, LA(M), a zone-edge mode, activated by disorder, was also identified in these spectra [21]. The  $A_{1g}(\Gamma)$  mode frequencies were observed at  $424.00$ ,  $422.13$ , and  $423.38$   $\text{cm}^{-1}$  while that of  $E_{2g}^1(\Gamma)$  modes were observed at  $356.84$ ,  $356.84$ , and  $359.32$   $\text{cm}^{-1}$ , for the films  $P_2$ ,  $P_3$  and  $P_4$ , respectively, while  $P_1$  film did not show any sign of Raman mode (as discussed in FESEM analysis). The peak position differences of the two Raman modes were  $\sim 67.16$ ,  $65.29$ , and  $64.06$   $\text{cm}^{-1}$ , indicating bulk-like to multilayered  $\text{WS}_2$  films formation [22]. In the present case, as compared to the other reported PLD and CVD  $\text{WS}_2$  films [22, 35], an unusual blue shift by  $\sim 2$ – $4$   $\text{cm}^{-1}$  for  $A_{1g}(\Gamma)$  mode and  $\sim 1.5$ – $4$   $\text{cm}^{-1}$  for  $E_{2g}^1(\Gamma)$  mode was observed. This blueshift in Raman modes indicates the presence of strain in the films. All Raman modes showed an unusual broadening compared with the Raman spectra of CVD growth  $\text{WS}_2$  films [8, 35]. To get detailed picture of the anomalous Raman vibrational modes, the spectrum of  $\text{WS}_2$  film deposited at high vacuum ( $P_4$ ) was deconvoluted into multiple Gaussian peaks.

The strongest peak at  $\sim 359.32$   $\text{cm}^{-1}$  was resolved into three individual contributions at  $358.6$ ,  $349.4$ , and  $341.1$   $\text{cm}^{-1}$  as shown in Fig. 2b. These modes were assigned as the in-plane vibrational  $E_{2g}^1(\Gamma)$  mode, the second-order longitudinal acoustic phonon 2LA (M) mode, and the in-plane vibrational  $E_{2g}^1(\text{M})$  mode, respectively [22, 23]. The other peak at  $423.5$   $\text{cm}^{-1}$

was attributed to the out-of-plane  $A_{1g}$  mode. Along with all these well-established Raman vibration modes, a large numbers of unknown peaks were also observed in the deconvoluted spectra. This indicated the existence of defects (as discussed in TEM analysis) arising from the disorder in the atomic arrangement of the  $WS_2$  film due to low deposition temperature and fast cooling rate. The thicknesses of the  $WS_2$  films  $P_1$ ,  $P_2$ ,  $P_3$ , and  $P_4$  were measured by stylus profilometer as  $\sim 10.8$ ,  $35.1$ ,  $38.2$ , and  $29.2$  nm, respectively.

Figure 3a, b shows the XRD spectra of  $WS_2$  pellet and all the  $WS_2$  films, respectively. XRD peaks corresponding to the  $WS_2$  crystalline planes (002), (004), (100), (101), (103), (006), (105), (110), (008), and (112) were observed in XRD pattern of the  $WS_2$  pellet. On the other hand, no significant XRD peaks were observed in  $P_1$  film. The thickness of the film was only a few nm ( $\sim 10.8$  nm, as measured by surface profilometer) which is very less compared to the other films. The film was also highly nonstoichiometric (as discussed in EDX analysis) compared to

the other films. Hence, the signature of  $WS_2$  structure was too weak to produce XRD pattern, and as a result, no significant XRD peaks were observed in this film. The  $P_2$ ,  $P_3$ , and  $P_4$  films showed XRD peaks at  $2\theta \sim 12.26^\circ$ ,  $40.25^\circ$ , and  $44.05^\circ$  corresponding to the (002), (103), and (006) plane of  $WS_2$  crystal [22, 36]. An enlarged view (from  $30^\circ$  to  $55^\circ$  of  $2\theta$ ) of the XRD spectra of the  $WS_2$  films is shown in the inset of Fig. 3b. (110) plane of W also possesses XRD peak at  $2\theta \sim 40.25^\circ$  [37, 38]. Along with  $WS_2$  structure, the films may contain metallic W, which was confirmed later by TEM and EDX analysis. For (002) plane of  $WS_2$ , the peak was shifted to a lower  $2\theta$  value by  $2.03^\circ$  as compared to the bulk ( $2\theta \sim 14.29^\circ$  for (002) plane) counterpart [39]. Hence, the shift of peak position of (002) plane to lower  $2\theta$  value suggested that the  $WS_2$  films experienced out-of-plane tensile strain. XRD peaks corresponding to the  $WS_2$  (002) plane of all the films also showed broad FWHM which may be the cause of  $WS_2$  nanocrystallite formation.

The crystallite sizes of the films were estimated by applying the Debye Sherrer formula, defined as,  $D = \frac{0.89\lambda}{\beta \cos\theta}$ , where  $D$ ,  $\lambda$ , and  $\beta$  are the average crystallite size, X-ray wavelength, and full width at half maxima (FWHM) of XRD peak, and  $\theta$  is the diffraction angle of the corresponding XRD peak. The average crystallite size of the  $WS_2$  films was determined corresponding to the (002) plane orientation. The crystallite size of the  $P_2$ ,  $P_3$ , and  $P_4$  films were estimated to be 4.1, 4.3, and 3.8 nm, respectively, which suggested  $WS_2$  nanocrystallite formation in every case.

Zabinski et al. also observed almost similar sized  $WS_2$  crystalline domain ( $< 2$  nm) formation in PLD deposited  $WS_2$  films at room temperature [40]. The present result suggests that irrespective of the deposition Ar gas pressures,  $WS_2$  nanocrystallites were formed throughout the film. In addition, the lattice parameters of the  $WS_2$  nanocrystallite were estimated using the following plane spacing equation for the hexagonal structure and Bragg's law

$$\frac{1}{d^2} = \frac{4}{3} \left( \frac{h^2 + hk + k^2}{a^2} \right) + \frac{l^2}{c^2} \quad \text{and} \quad 2d \sin \theta = \lambda \quad (1)$$

where  $d$  is the inter-planar spacing,  $(h, k, l)$  are the Miller indices,  $a$  and  $c$  are the lattice parameters,  $\theta$  is the scattering angle, and  $\lambda$  is the X-ray wavelength. Crystallite size ( $D$ ), inter-planar spacing ( $d_{hkl}$ ) and

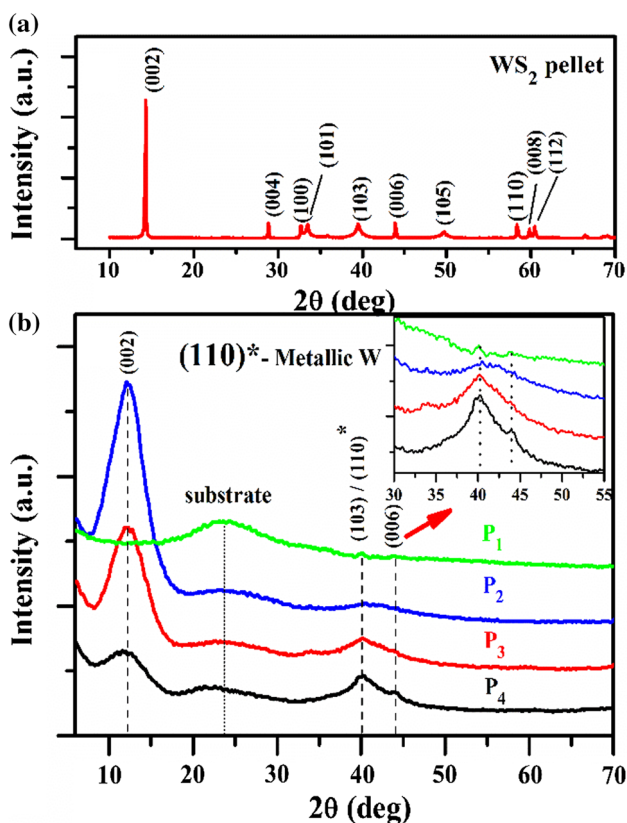


**Figure 3** XRD spectra of **a**  $WS_2$  pellet and **b**  $WS_2$  films deposited at various argon pressures.



lattice constants ( $a$  and  $c$ ) of the  $WS_2$  thin films estimated from Eq. (1) are listed in Table 1.

From the table, we observe that for all the  $WS_2$  films, lattice parameter ' $a$ ' shortened and ' $c$ ' elongated compared to the bulk counterpart, i.e., all the films experienced an in-plane compressive strain and out-of-plane tensile strain.

Further, FETEM images of the  $WS_2$  film were analyzed to unveil the nanostructure and crystallinity at nano scale. Figure 4a–c shows the FETEM image of the  $P_4$  film of various magnifications. At higher magnification, nanosize core-shell structures were observed which were sparsely distributed throughout the film. The core area was metallic W covered by semiconductor  $WS_2$  shell as confirmed by EDX analysis. Figure 4d shows the HRTEM image of a certain position of the film where we found that crystalline nanoclusters were embedded in the amorphous  $WS_2$  film. From the HRTEM image,  $d$ -spacing of  $\sim 0.224$  nm was estimated which corresponds to W [110] or  $WS_2$  [103] plane. The crystallite size corresponding to the  $WS_2$  [103] plane was observed to be 5–8 nm. Figure 4e shows the FFT image of the rectangular selected region in the HRTEM image. From the FFT image, it was observed that the  $d$ -spacing line was distorted in some regions corresponding to the stress and strain in the film. A bright and dark color contrast was also observed in the FFT presentation. Hence, crystals contain point defects, like atomic vacancy, i.e., a missing atom (S atomic vacancy as confirmed by EDX analysis) caused distortion in lattice planes in the immediate vicinity of the atomic vacant position. The local strain created by the cluster of vacancies of S atom (a small void) gave rise to the characteristic bright/dark diffraction contrast.

Figure 4f shows the SAED pattern of the film where multiple diffuse rings were observed corresponding to the polycrystalline nature of the film. Along with the  $WS_2$  structure, the excess W also created bright circular rings in SAED pattern. [100], [103] planes of  $WS_2$  and [110], [200], [211], [220], [310],

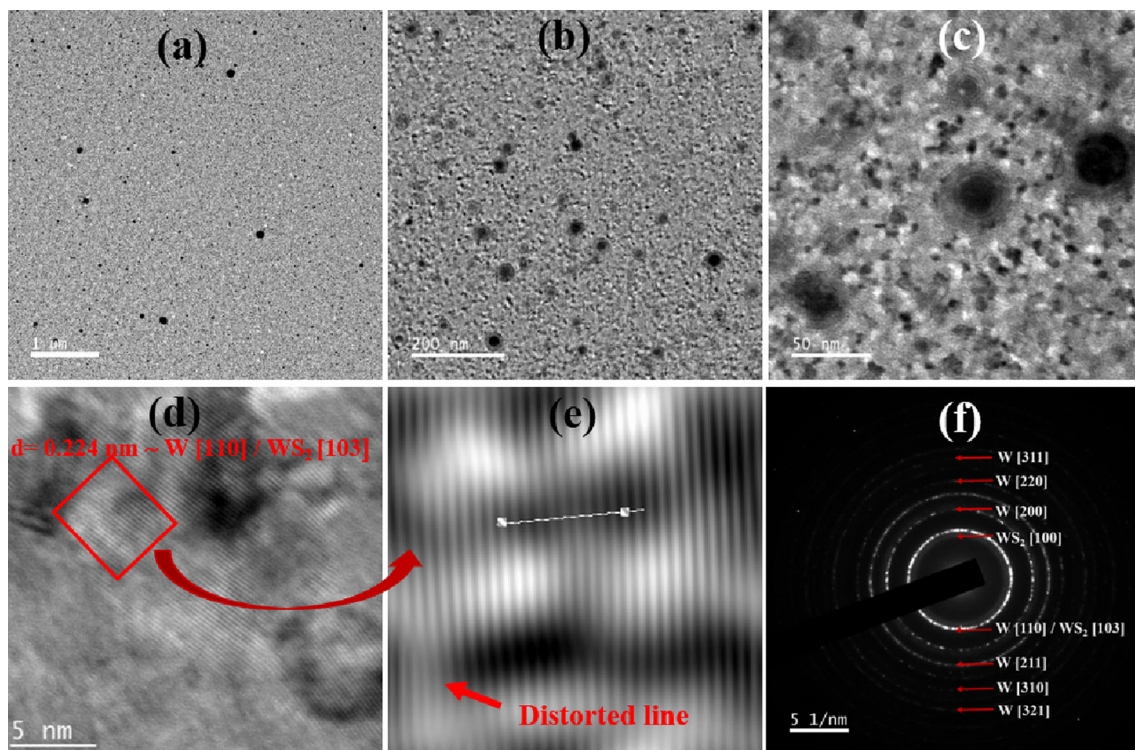
[311], and [321] planes of W were detected from SAED pattern. So, HRTEM and SAED analysis confirmed a mixed  $WS_2$  and W structure formation throughout the film.

Figure 5a–d shows EDX spectra of  $WS_2$  thin films  $P_1$ ,  $P_2$ ,  $P_3$ , and  $P_4$ , respectively. Atomic % of each element of  $WS_2$  is presented in the inset of every figure. The atomic percentage of S was observed to be  $\sim 48.1$ , 63.3, 58.7, and 56.6% for the  $WS_x$  thin films corresponding to  $x = 0.93$ , 1.72, 1.42, and 1.30, deposited at Ar pressure of  $10^{-1}$  ( $P_1$ ),  $10^{-2}$  ( $P_2$ ),  $10^{-3}$  ( $P_3$ ), and  $10^{-5}$  ( $P_4$ ) mbar, respectively. Irrespective of the deposition Ar pressure, S deficiency was observed in each film. Hence among various deposition pressures, S atomic % in the  $WS_2$  films mostly reduces at high vacuum ( $10^{-5}$  mbar) and high Ar pressure ( $10^{-1}$  mbar) conditions. During the deposition, the lighter S atoms get diffuse in a larger area for the film deposited at lowest pressure while the S atoms are restricted in moving forward at high pressure causing a high S deficiency in the  $WS_2$  films. In the present case, instead of forming  $WO_x$  structure, the excess W present in the film remained as metallic W in the film as the signature of  $WS_2$  and W was only detected in XRD, Raman, and TEM measurement. This huge S-atomic deficiency created atomic vacancy in the films which caused lattice distortion in  $WS_2$  crystalline structure and left excess metallic tungsten (W) onto the film as observed previously in HRTEM image and SAED pattern. The S deficiency also created a large number of defect states in  $WS_2$  structure as previously observed in Raman spectra. Similar excess metallic tungsten (W) was also detected in almost all the PLD deposited  $WS_2$  films [22, 25, 40, 41].

Figure 6 shows AFM images of all the  $WS_2$  films. Surface topology of the films showed nanocluster formation throughout the films. A large number of nanoparticles were distributed throughout the  $P_1$  and  $P_4$  films while the surfaces of films  $P_2$  and  $P_3$  were free from all the nanoparticles. RMS roughness

**Table 1** Crystallite size ( $D$ ), inter-planar spacing ( $d_{hkl}$ ) and lattice constants ( $a$  and  $c$ ) of  $WS_2$  pellet and  $WS_2$  thin films deposited at various Ar gas pressure

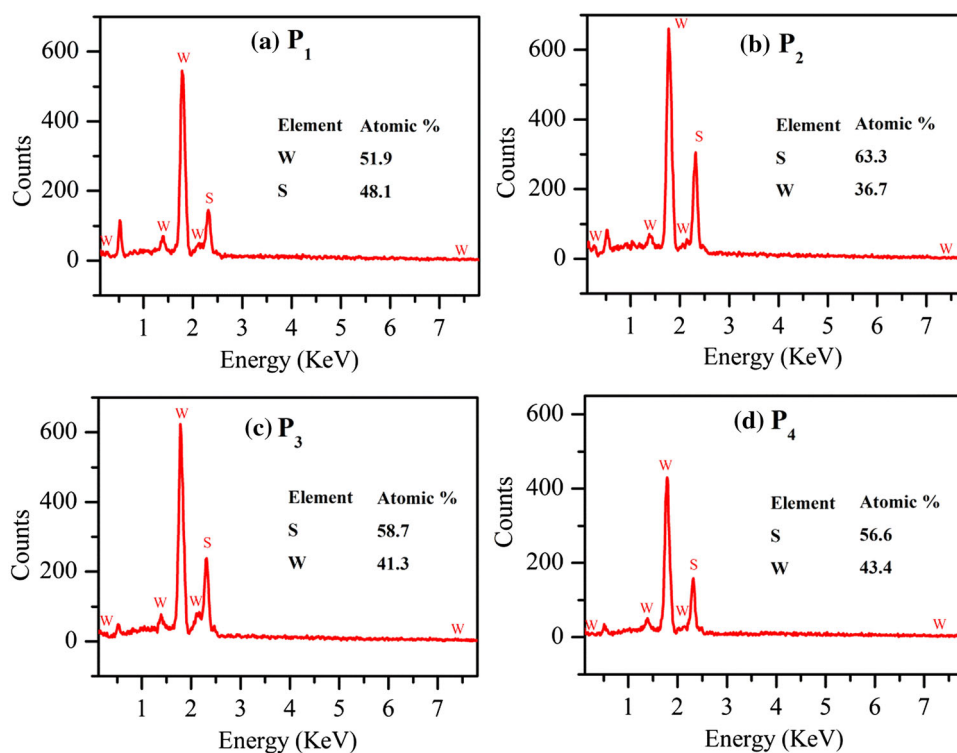
Sample	Crystalline size, $D_{002}$ (nm)	$d_{002}$ (nm)	$d_{103}$ (nm)	$a$ (nm)	$c$ (nm)
$WS_2$ pellet	123.8	0.613	0.228	0.317	1.226
$P_2$	4.1	0.721	0.223	0.289	1.443
$P_3$	4.3	0.716	0.224	0.290	1.432
$P_4$	3.8	0.720	0.224	0.292	1.439



**Figure 4** a–c FETEM images at various magnification of sample P<sub>4</sub>. **d** The HRTEM image of the film shows nanocluster formation over the amorphous film background. **e** FFT of the nanocrystallites

with *d*-spacing as extracted from HRTEM image using Gatan software. **f** SAED pattern of the film which shows the presence of polycrystalline W and WS<sub>2</sub>.

**Figure 5** EDX spectra and W and S atomic ratio (%) of the WS<sub>2</sub> films **a** P<sub>1</sub>, **b** P<sub>2</sub>, **c** P<sub>3</sub> and **d** P<sub>4</sub>, respectively.



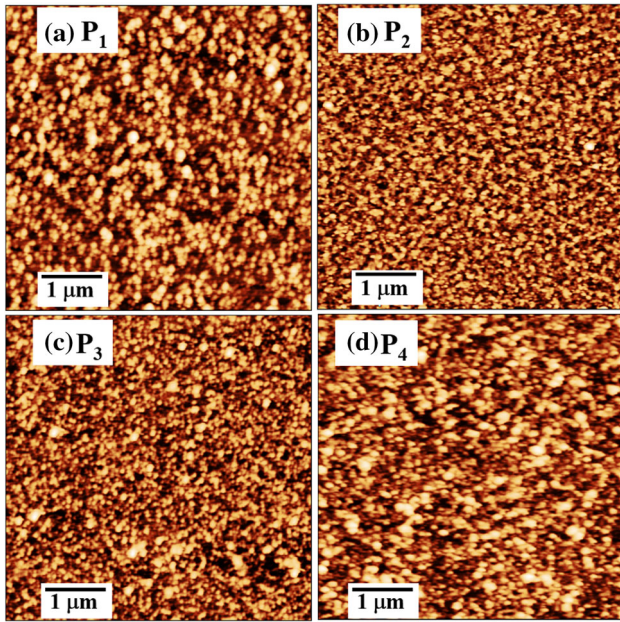


**Figure 6** AFM images of surface topology of the WS<sub>2</sub> films **a** P<sub>1</sub>, **b** P<sub>2</sub>, **c** P<sub>3</sub> and **d** P<sub>4</sub>, respectively.

values of the films were 6.6, 4.2, 4.8, and 8.4 nm corresponding to the P<sub>1</sub>, P<sub>2</sub>, P<sub>3</sub>, and P<sub>4</sub> films, respectively.

Surface morphology of the film was further investigated by the analysis of FESEM images. Figure 7 shows the FESEM images of all the WS<sub>2</sub> films. It is observed that small circular nanoclusters of metallic tungsten (W) (in bright white color) were distributed throughout the films where the density of the clusters were higher in the P<sub>1</sub> and P<sub>4</sub> films [25]. In the EDX analysis, high density of metallic W was also observed in the P<sub>1</sub> and P<sub>4</sub> films compared to the other films. The presence of dense metallic W nanoclusters onto the top surface depressed the Raman and XRD signal of the underlying WS<sub>2</sub> films as observed earlier. Similar surface morphology was also observed in the AFM images presented in Fig. 6.

The spectroscopic ellipsometry (SE) measurement was performed to explore the linear optical behavior of the WS<sub>2</sub> films. SE measurement is a nondestructive and noncontact technique to extract the optical properties of thin films by modeling the optical response of the material. The optical parameters were extracted by fitting the SE spectra of the respective WS<sub>2</sub> films. The experimentally measurable ellipsometric parameters  $\psi$  represent amplitude ratio of  $p$  and  $s$  component of the reflected light and  $\Delta$  corresponds to the phase difference of  $p$  and  $s$  component.

They are related as:  $\rho = r_s/r_p = \tan \psi \exp(j\Delta)$ , where  $r_p$  and  $r_s$  are the complex reflection coefficients of parallel and perpendicular component of reflected polarized light from WS<sub>2</sub> film surface [42]. The ellipsometer measurement was performed at 70° angle of incidence of the plane polarized light. The recorded spectra were fitted with an effective dispersion model with the help of Spectroscopy ellipsometry analyzer (SEA) software. To fit the recorded spectra a four-layer model consisting of glass/WS<sub>2</sub>/WS<sub>2</sub> rough surface/ambient air was considered (schematically presented in Fig. 8a) where glass is the substrate, WS<sub>2</sub> is the film deposited on the substrate, and the fourth layer is the air medium above the film. During simulation, pre-calculated  $nk$ -file data was used for glass substrate and ambient air. The thickness of glass substrate was 1 mm. WS<sub>2</sub> film upper surface roughness was analyzed by applying Bruggeman-effective medium approximation (EMA) consisting of a mixed state of 50% WS<sub>2</sub> and 50% voids. Modified Forouhi–Bloomer (MFB) dispersion model was used to fit the experimental Spectra. MFB model was developed by considering the effect of non-parabolic energy dependence of valence and conduction bands of semiconductor material. It provides more accurate optical constant of mostly amorphous semiconductor and dielectric materials [43]. The refractive index ( $n$ ) and absorption coefficient ( $k$ ) corresponding to the MFB model are as follows [44, 45]

$$n(E) = \frac{-(B_0D + 2C_0)E + 2B_0F + C_0D}{(E - D)E + F} \quad \text{and} \quad (2)$$

$$k(E) = \frac{A + B(E - E_g) + C(E - E_g)^2}{(E - D)E + F}$$

Here  $B_0$  and  $C_0$  are given by  $B_0 = \frac{B - 2CE_g + CD}{\sqrt{4F - D^2}}$  and  $C_0 = \frac{A - BE_g + CE_g^2 - CF}{\sqrt{4F - D^2}}$ , where the law parameters  $A, B, C, D$  and  $F$  have positive nonzero values and  $E_g$  represents the optical energy bandgap in eV.

Hence,  $n$  and  $k$  or real and imaginary dielectric constant ( $\epsilon_1$  and  $\epsilon_2$ ) are function of  $\psi$  and  $\Delta$  and can be extracted from SE recorded spectra of  $\tan \psi$  and  $\cos \Delta$ . In the present case, experimentally measured SE spectra ( $\epsilon_1$  and  $\epsilon_2$ ) of the WS<sub>2</sub> films were fitted with simulated MFB model as shown in Fig. 8b, c. During simulation, Levenberg–Marquardt nonlinear regression algorithm was applied to minimize the error in fitting of the SE spectra. The root-mean-square error (RMSE) presents the goodness of the fit. In our case,



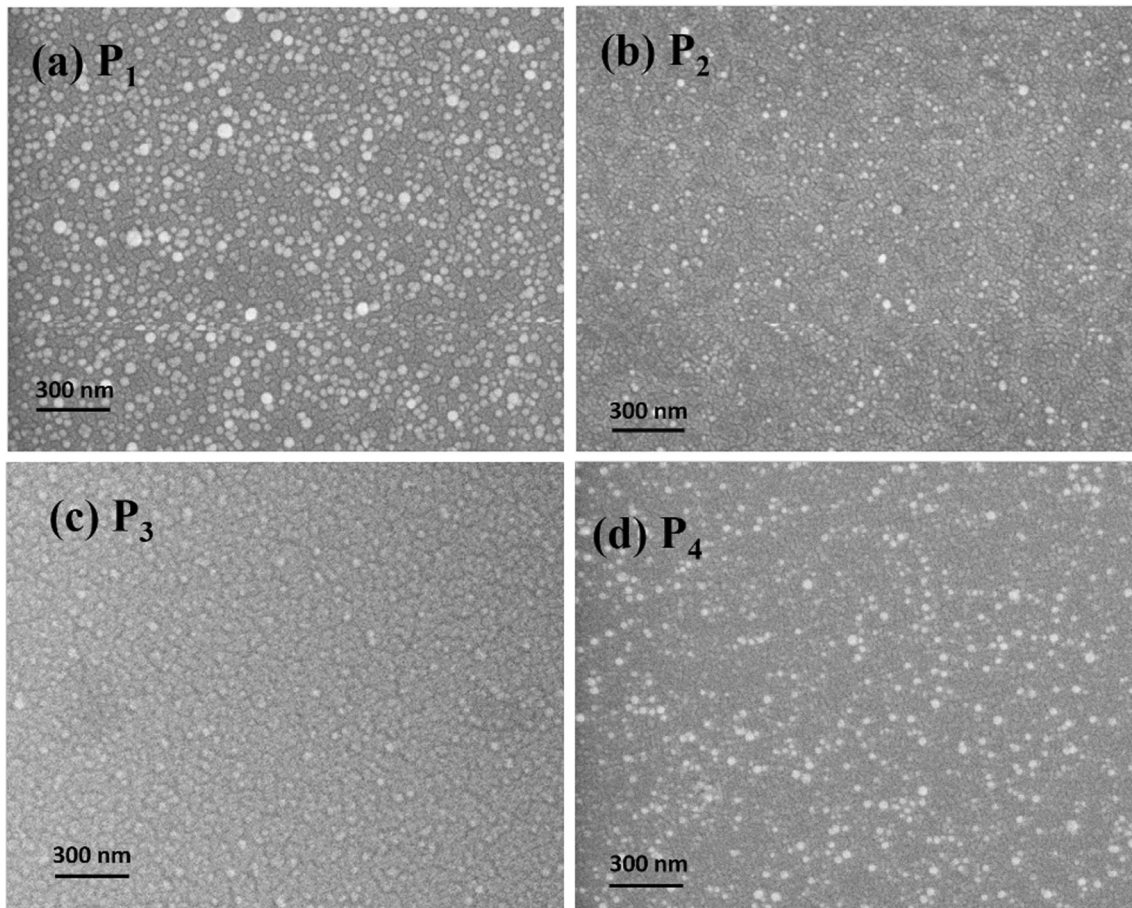
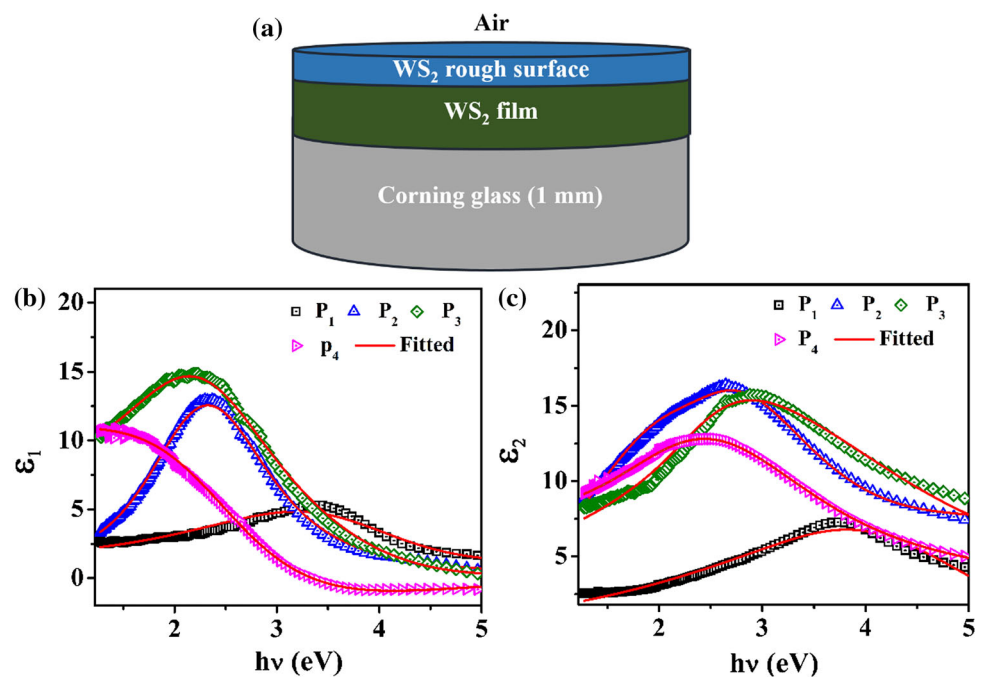


**Figure 7** FESEM images of the  $WS_2$  films **a**  $P_1$ , **b**  $P_2$ , **c**  $P_3$  and **d**  $P_4$ , respectively.

**Figure 8 a** Schematic of four-layered model considered for the ellipsometer fitting. The plot of recorded ellipsometer spectra fitted with simulated dispersion law spectra in terms of **b**  $\epsilon_1$  and **c**  $\epsilon_2$ .





the RMSE values were 0.02–0.05 ( $\sim 0$ ), suggesting a good fit of the simulation result with the measured one. The measured  $\epsilon_1$  and  $\epsilon_2$  spectra did not show any excitonic transition peaks corresponding to A/B or C/D excitonic transitions of layered WS<sub>2</sub> films, while a broad peak was observed in every spectrum.

The  $\epsilon_2$  spectra of the films showed peak positions in the range of  $\sim 2.5$ – $3.75$  eV where the value of  $\epsilon_2$  of the P<sub>2</sub> and P<sub>3</sub> films were high compared to the other films because of high thickness of the respective films. Quantum confinement effect due to the nanocrystallite WS<sub>2</sub> may cause the shift in peak positions to higher energy, while defect states in the WS<sub>2</sub> structure cause the huge broadening in the spectra of  $\epsilon_1$  and  $\epsilon_2$ . Through the best fitting of experimental  $\epsilon_1$  and  $\epsilon_2$  spectra, various important parameters like film thickness ( $d$ ), surface roughness ( $r$ ) and optical parameters like refractive index ( $n$ ), and extinction coefficient ( $k$ ), were extracted efficiently. The thickness and RMS roughness of the P<sub>1</sub>–P<sub>4</sub> films, estimated from SE analysis, were found to be  $\sim 12, 33, 39$  and  $27$  nm and  $6.5, 3.4, 5,$  and  $8.7$  nm, respectively, which were similar to that of measured thickness from profilometer and extracted RMS roughness from AFM images.  $n$  and  $k$  spectra of the films, extracted from ellipsometer fitting are shown in Fig. 9a, b. No significant absorption peak in  $k$  spectra was observed in infrared to visible regions, while a strong absorption was observed at 300–350 nm region. Salman et al. also observed an absorption peak around  $\sim 3.5$  eV ( $\lambda \sim 350$  nm) in a PLD WS<sub>2</sub> film containing metallic W droplets [41].

Further, the absorption coefficient ( $\alpha$ ) of the WS<sub>2</sub> films was extracted from the ellipsometric extinction coefficient from the relation,  $\alpha = (4\pi k/\lambda)$ , ( $\lambda$  is the optical wavelength) as shown in the inset of Fig. 10. The optical bandgap of the respective WS<sub>2</sub> films can

**Figure 9** The plot of **a**  $n$  and **b**  $k$  spectra of the WS<sub>2</sub> films extracted from the ellipsometer analysis.

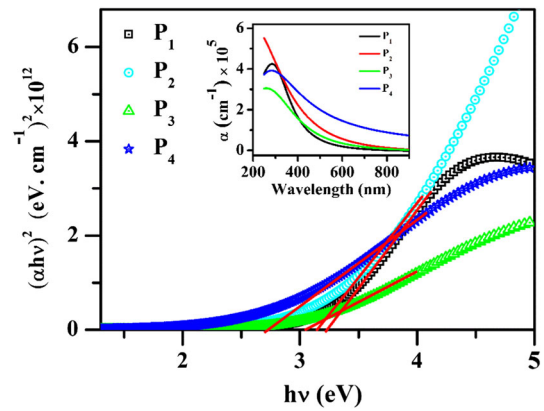
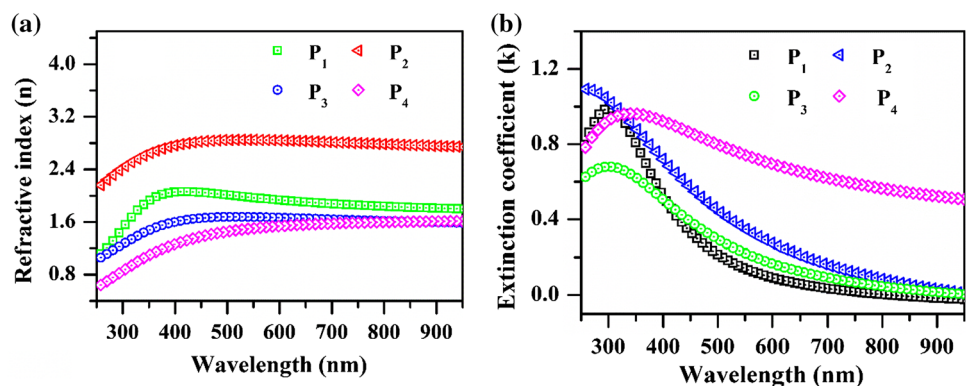


**Figure 10** Tauc plot  $[(\alpha hv)^2$  vs.  $hv$ ] and direct bandgap estimation of the WS<sub>2</sub> films.

be estimated by applying Tauc plot. The Tauc plot is presented as  $(\alpha hv)^{1/n} = K(hv - E_g)$  where,  $hv$  is the photon energy,  $K$  is a constant and  $n$  is a number characterize the band transition processes. The number  $n = 1/2$  characterize direct band transition while  $n = 2$  corresponds to indirect band transition. Figure 10 shows the Tauc plot of the respective WS<sub>2</sub> films which demonstrated a direct bandgap in the region of 2.7–3.25 eV, which is quite high compared to the layered WS<sub>2</sub> films, attributed to the quantum confinement effect [46, 47].

Figure 11 shows absorbance spectra of WS<sub>2</sub> thin films, measured by UV–Vis spectroscopy. The optical absorption spectrum shows a minimum optical spectrum shows a minimum optical absorption feature at higher wavelength region and a strong rise in absorption was observed in the UV region. From 800 to 300 nm P<sub>2</sub> and P<sub>3</sub> films show higher absorbance than the rest. The comparatively high thickness of the films may result in higher absorbance or the presence of W in the P<sub>1</sub> and P<sub>4</sub> films may lead to reflection of the incident light and lower the absorbance. Almost all spectra showed a

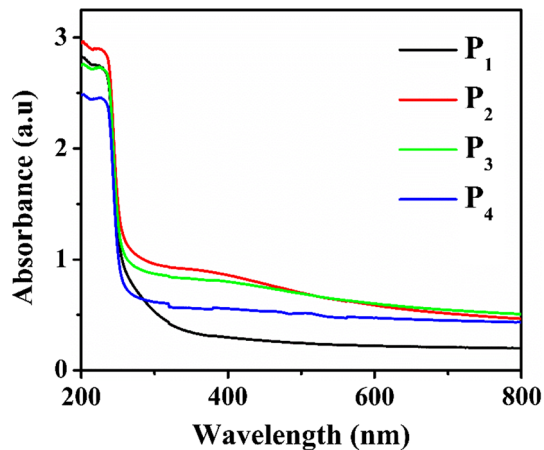


**Figure 11** Plot of UV-Vis absorbance spectra of all the WS<sub>2</sub> films.

sharp rise in absorption at  $\sim 250$  nm. Unlike the optical properties of other CVD-grown WS<sub>2</sub> thin films [48] and WS<sub>2</sub> nanosheets from the PLA technique in DI water, the excitonic absorption peaks corresponding to A/B and C/D excitonic transitions disappeared in these absorption spectra. Hence, the WS<sub>2</sub> nanocrystals behaved like quantum dots resulting in the band edge shifts to a shorter wavelength [46, 47].

The NLA and NLR coefficient of the WS<sub>2</sub> films were obtained by fitting the open- and close-aperture transmitted beam of different position with the respective position-dependent transmitted intensity formulae. The transmittance beam passes through the sample express as [20, 49]

$$T_{\text{op}} = 1 - \frac{c}{(1 + bz^2)} \quad (3)$$

$$T_{\text{cl}} = 1 + \frac{4az}{(1 + bz^2)(9 + bz^2)} \quad (4)$$

where  $T_{\text{op}}$  and  $T_{\text{cl}}$  are normalized transmission for open-aperture Z-scan and close-aperture Z-scan,  $c = \beta I L_{\text{eff}} / 2^{3/2}$ ,  $a = 2\pi n_2 I L_{\text{eff}} / z_0$ ,  $b = 1/z_0^2$ ,  $\beta$  and  $n_2$  represent the nonlinear absorption coefficient and nonlinear refractive coefficient of the sample,  $I$  is the intensity of the laser beam at focus point,  $z_0$  is the Rayleigh length, and  $L_{\text{eff}}$  is the effective thickness of the WS<sub>2</sub> film which is given by equation

$$L_{\text{eff}} = \frac{1 - \exp(-\alpha L)}{\alpha} \quad (5)$$

where  $\alpha$  and  $L$  are the linear absorption coefficient and average film thickness, respectively. The value of  $L$ , measured by ellipsometer, was found to be 12, 33, 39, and 27 nm in the films P<sub>1</sub>–P<sub>4</sub>, respectively.

Further, the linear absorption coefficient ( $\alpha$ ) at the laser wavelength (632.8 nm) was extracted from the UV-Vis spectra (Fig. 9b) of the respective films.

Figure 12a–c shows the measured open-aperture Z-scan transmitted beam fitted with Eq. (3). The transmitted beam showed valley at the focused point followed by a symmetric structure with respect to the center ( $z = 0$ ), i.e., the films showed reverse saturation absorption (RSA). The incident laser beam photon energy was 1.96 eV (632.8 nm) which was much less than the optical band gap (2.7–3.25 eV) of the films as measured from Tauc plot. So ‘two-photon absorption’ (2PA) by WS<sub>2</sub> nanocrystals was the primary cause of RSA phenomenon of the films. 2PA induced RSA was also reported in Zn<sub>1-x</sub>Al<sub>x</sub>O thin films of band gaps 3.26–3.64 eV, measured by Z-scan under He–Ne laser source [50]. Along with WS<sub>2</sub> nanocrystals, metallic W may also contribute to the nonlinear absorption by interband transition of bound electron (from  $d$  band to  $s$ - $p$  bands) and intraband transition of conduction electrons (due to the dipole oscillations of the free electrons) and partially absorbing the cw laser produced thermal heating [51]. Ningning et al. and Zin et al. also reported RSA in monolayer WS<sub>2</sub> (bandgap  $\sim 2.1$  eV) by 2PA of femtosecond laser pulse of wavelength 800 ( $\sim 1.55$ ) and 1040 nm ( $\sim 1.19$  eV) [27, 52]. The nonlinear absorption coefficient,  $\beta$ , was calculated from the normalized transmittance data of the open-aperture Z-scan measurement after being fitted to Eq. (3). Further  $n_2$  of the films were extracted by fitting Eq. (4) with the close-aperture transmission beam as shown in Fig. 12d–f. It was observed that the closed-aperture transmission beams possess valley (transmission minimum) before the focus position and a peak (transmission maximum) after the focus position. This valley–peak position in the closed-aperture transmission beam due to the self-focusing phenomenon of the film which corresponds to the positive nonlinear refractive index ( $n_2$ ) of WS<sub>2</sub> films.

The real ( $\chi_R^3$ ) and imaginary ( $\chi_I^3$ ) third-order nonlinear optical susceptibility of the WS<sub>2</sub> films can be obtained using the following equations [20]

$$\chi_R^3 = 10^{-7} \frac{nc}{12\pi^2} (nn_2 - kk_2) \quad (6)$$

$$\chi_I^3 = 10^{-7} \frac{nc}{12\pi^2} (nk_2 + kn_2) \quad (7)$$

and corresponding third-order nonlinear optical susceptibility ( $\chi^3$ ) is

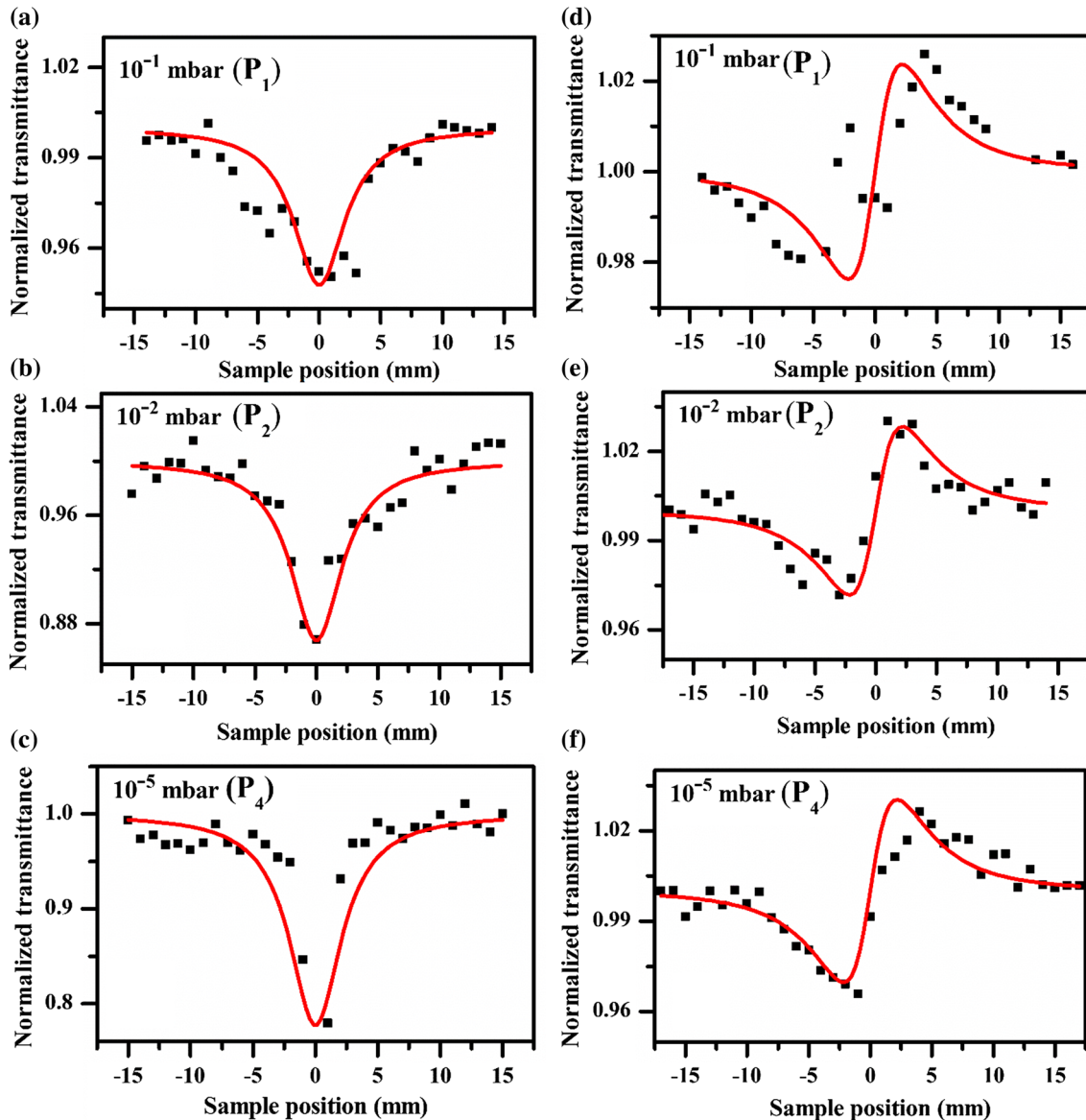


**Figure 12** The plot of open Z-scan normalized transmission intensity of the films **a** P<sub>1</sub>, **b** P<sub>2</sub>, and **c** P<sub>4</sub>. The plot of closed Z-scan normalized transmission intensity of the films **d** P<sub>1</sub>, **e** P<sub>2</sub>, and **f** P<sub>4</sub>, respectively.

$$\chi^3 = \sqrt{(\chi_R^3)^2 + (\chi_I^3)^2} \tag{8}$$

where  $n$  is the linear refractive index,  $k$  ( $= \frac{\alpha\lambda}{4\pi}$ ) is the linear extinction coefficient and  $k_2$  ( $= \frac{\beta\lambda}{4\pi}$ ) is the nonlinear extinction coefficient. The calculated values of  $n_2$ ,  $\beta$ ,  $\chi_R^3$ ,  $\chi_I^3$  and  $\chi^3$  of the WS<sub>2</sub> films are listed in Table 2.

A significantly large values of  $\beta$ ,  $n_2$ ,  $\chi_R^3$  and  $\chi_I^3$  were observed in the S-deficient nanocrystallites WS<sub>2</sub> films as compared to the reported nonlinear optical parameters of monolayer, multilayer, bulk-like WS<sub>2</sub>

films measured by Z-scan technique with a pulsed laser source (nano and femtosecond pulsed) [26, 27, 52].  $\beta$  and  $n_2$  of the WS<sub>2</sub> films were found 10<sup>5</sup> times larger than that of monolayer WS<sub>2</sub> under fs-pulsed laser irradiation as reported by Zin et al. [27], whereas  $\chi_R^3$  and  $\chi_I^3$  in present work are 10<sup>6</sup> and 10<sup>7</sup> times higher than that observed in monolayer WS<sub>2</sub> under fs-pulsed laser as reported by Ningning et al. [52].  $\chi^3$  was also found to be 10<sup>7</sup> times higher than the reported value in mono to multilayered WS<sub>2</sub> films under ns-pulsed laser by Carlos et al. [26]. However, similar order of  $(-)\beta$  and  $(-)n_2$  was observed in MoS<sub>2</sub>



**Table 2** Nonlinear optical coefficients ( $\beta$ ,  $n_2$ ,  $\chi_R^3$ ,  $\chi_I^3$  and  $\chi^3$ ) of WS<sub>2</sub> thin films deposited for 6 min at various Ar gas pressure

WS <sub>2</sub> films	Nonlinear refractive index, $n_2$ (cm <sup>2</sup> /W) $\times 10^{-4}$	Nonlinear absorption coefficient, $\beta$ (cm/W)	Real third-order susceptibility, $\chi_R^3$ (esu) $\times 10^{-2}$	Imaginary third-order susceptibility, $\chi_I^3$ (esu) $\times 10^{-2}$	Third-order susceptibility, $\chi^3$ (esu) $\times 10^{-2}$
P <sub>1</sub>	1.1	17.34	0.97	1.31	1.63
P <sub>2</sub>	1.67	27.40	3.02	2.05	3.65
P <sub>4</sub>	1.67	45.50	6.70	3.16	7.41

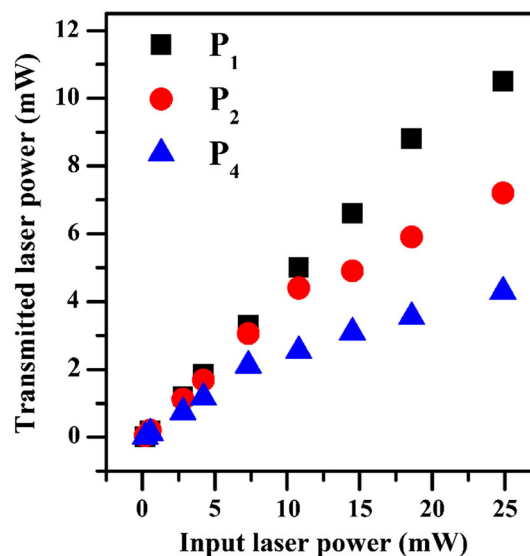
nanoflakes, where Z-scan measurement was performed under a diode laser source of wavelength 532 nm [53]. Hence, observed large values of NLO coefficients of the nc-WS<sub>2</sub> films in our work can be prompted by the high-energy excitonic states created by quantum confinement effects as well as by cw laser-induced heating effects. In quantum confinement region, the oscillator strength enhances and interaction of the local electric field of the light with nanostructures becomes stronger as observed earlier in nc-SiO<sub>x</sub> thin films [20].

In the present study, Z-scan experiment was performed under CW laser illumination, where the incident laser beam is absorbed by the optical material and induced considerable thermal heating in the samples. The high temperature of the illuminated portion of the material leads to a change in the NLO properties of the material. Hence thermally induced optical nonlinearities cause large NLO coefficients of the WS<sub>2</sub> films [50, 54]. In a high absorbing medium, the change in refractive index caused by laser heating process is expressed as [50],

$$\Delta n = \left(\frac{dn}{dT}\right) \left(\frac{w_0}{2}\right)^2 \left(\frac{I}{k}\right) \quad (9)$$

where  $k$  is coefficient of thermal conductivity of the optical material and  $w_0$  is the radius of the laser beam. Hence  $\Delta n$  itself comes out to be  $\sim 10^{-4}$  cm<sup>2</sup>/W for the current experimental setup which indicates that in case of CW laser the thermal nonlinearity dominates over optical nonlinearity.

Possessing a large nonlinear coefficient ( $\beta$ ) with RSA response, the WS<sub>2</sub> films may be effective as an optical limiter material. Figure 13 shows the characteristics optical limiting behavior of the WS<sub>2</sub> films measured by the Z-scan setup (as shown in Fig. 1) where the sample was placed at laser focused position ( $z = 0$ ) and the transmitted output power was measured with step-by-step increase in input laser power. From Fig. 13 it is clearly observed that initially the transmitted output power linearly varied

**Figure 13** Optical limiting response of the WS<sub>2</sub> thin films deposited at various Ar gas pressure.

with the input laser power but with further increase in laser power the output power gradually deviated from its linear behavior and moved toward saturation. The starting point of deviation from linear nature is referred to as optical limiting threshold point. It is observed that the threshold point is shifted from lower input laser energy to higher energy (4.2, 7.3 and 18.6 mW, respectively) with an increase in deposition pressure from  $10^{-5}$  to  $10^{-1}$  mbar. Hence the WS<sub>2</sub> film of higher  $\beta$  value appears as more efficient optical limiter material [28].

Although PLD technique is well known for deposition of stoichiometric thin films, in the present work all the PLD WS<sub>2</sub> films deposited at various Ar pressure were nonstoichiometric with huge S deficiency. Even similar nonstoichiometric WS<sub>2</sub> films were observed in most of the reported PLD WS<sub>2</sub> films irrespective of deposition conditions [22, 25, 40]. In PLD, during deposition, the laser ablated highly energetic plasma components bombarded on the pre-

deposited WS<sub>2</sub> film with a very high velocity of  $\sim 1.0 \times 10^3$ – $5.0 \times 10^4$  m/s and causes random diffusion and redistribution of the relatively light S atoms. As S possesses a very low boiling point of  $\sim 445$  °C, the heated substrate causes melting and re-evaporation of S from the substrate surface and creates S deficiency in the WS<sub>2</sub> films irrespective of deposition gas pressure. The presence of metallic tungsten (W) in WS<sub>2</sub> film was reported by Tamie et al. in WS<sub>2</sub> films grown by pulsed laser deposition. Rumaner et al. also observed similar WS<sub>2</sub> films as deposited by ion-assisted technique [22, 55]. The nonstoichiometry of the films affects greatly the film crystallinity as well as surface morphology. More the S deficiency in the film, smaller the crystalline size and larger the surface RMS roughness. The absence of S creates a discontinuity in the WS<sub>2</sub> films and generates WS<sub>2</sub> nanocrystallites throughout the film surface.

There are many reports on linear optical properties, nonlinear optical behavior of WS<sub>2</sub> thin films, nanoflakes, etc. [26, 27, 56]. So far, to the best of our knowledge, the linear and nonlinear optical behavior of S-deficient WS<sub>2</sub> thin films is not explored in detail. In the present work, we have systematically varied the W to S atomic ratio in WS<sub>2</sub> films under various deposition conditions and observed its effect on the linear and nonlinear optical properties of the respective films. The *as*-deposited WS<sub>2</sub> films showed a peculiar linear and nonlinear optical response compared to the reported optical properties of layered WS<sub>2</sub> thin films. The formation of WS<sub>2</sub> nanocrystallite of sizes within the quantum dot regime caused a shift in band gap to higher energy (2.7–3.25 eV) as compared to the layered WS<sub>2</sub> films ( $\leq 2.1$  eV). Hence, the high direct band gap (2.7–3.25 eV) of the nc-WS<sub>2</sub> films caused two-photon absorption of the exciting He–Ne laser beam (1.96 eV) and showed reverse saturation absorption with a high nonlinear refraction coefficient and large third-order nonlinear optical susceptibility. From the application point of view, the WS<sub>2</sub> films show its effectiveness as an optical limiter material (as shown in Fig. 13). The primary application of the optical limiter is protecting sensors or detectors from high energy irradiance. Furthermore, the S vacancy increases the active points in the films which makes it as active catalyst for photo-catalytic and hydrogen evolution reactions.

## Conclusion

WS<sub>2</sub> films were deposited using PLD technique at various Ar gas pressures. Irrespective of the deposition pressure huge S deficiency was observed in all the films. XRD and TEM analysis of the films shows that WS<sub>2</sub> nanocrystals formation along with W metal. A huge broadening in Raman and XRD spectra suggested a large number of defects created throughout the films. The S-deficient, nc-WS<sub>2</sub> films showed interesting linear and nonlinear optical properties, studied by UV–Vis, spectroscopic ellipsometer and Z-scan measurement. WS<sub>2</sub> nanocrystals formation of quantum dot sizes (4–8 nm) throughout the film caused a huge shift in band gap to higher energy and was observed near to 2.7–3.25 eV as confirmed by Tauc plot. Furthermore, the third-order optical nonlinearity of the WS<sub>2</sub> films was measured by Z-scan setup with a He–Ne laser source. All the films showed nonlinear reverse saturation absorption ( $\beta$ ) and positive nonlinear refractive index ( $n_2$ ) corresponding to the two-photon absorption by WS<sub>2</sub> nanocrystals and high thermal absorption rate of the incident laser beam by metallic W. CW laser-induced thermal nonlinearity dominated over optical nonlinearity and caused a large value in the nonlinear optical parameters like  $n_2$ ,  $\beta$  and  $\chi^3$ . Optical limiting was observed in WS<sub>2</sub> films where the limiting threshold power increased with increasing Ar gas pressure due to decrease in  $\beta$ .

## Acknowledgements

The authors acknowledge CIF, IIT Guwahati for micro-Raman, FETEM, AFM, FESEM and spectroscopic ellipsometer facilities. The authors also acknowledge department of Physics, IIT Guwahati, for XRD and UV–Vis facilities.

## Compliance with ethical standards

**Conflict of interest** The author(s) declares no competing interests.

## References

- [1] Gan X, Shiue R-J, Gao Y, Meric I, Heinz TF, Shepard K, Hone J, Assefa S, Englund D (2013) Chip-integrated

- ultrafast graphene photodetector with high responsivity. *Nat Photonics* 7(11):883–887
- [2] Shelke NT, Karche B (2017) Ultraviolet photosensor based on few layered reduced graphene oxide nanosheets. *Appl Surf Sci* 418:374–379
- [3] Mas-Balleste R, Gomez-Navarro C, Gomez-Herrero J, Zamora F (2011) 2D materials: to graphene and beyond. *Nanoscale* 3(1):20–30
- [4] Butler SZ, Hollen SM, Cao L, Cui Y, Gupta JA, Gutiérrez HR, Heinz TF, Hong SS, Huang J, Ismach AF (2013) Progress, challenges, and opportunities in two-dimensional materials beyond graphene. *ACS Nano* 7(4):2898–2926
- [5] Beshkova M, Hultman L, Yakimova R (2016) Device applications of epitaxial graphene on silicon carbide. *Vacuum* 128:186–197
- [6] Wang G, Dang S, Zhang P, Xiao S, Wang C, Zhong M (2017) Hybrid density functional study on the photocatalytic properties of AlN/MoSe<sub>2</sub>, AlN/WS<sub>2</sub>, and AlN/WSe<sub>2</sub> heterostructures. *J Phys D* 51(2):025109
- [7] Liu X, Hu J, Yue C, Della Fera N, Ling Y, Mao Z, Wei J (2014) High performance field-effect transistor based on multilayer tungsten disulfide. *ACS Nano* 8(10):10396–10402
- [8] Elías AL, Perea-Lopez N, Castro-Beltran A, Berkdemir A, Lv R, Feng S, Long AD, Hayashi T, Kim YA, Endo M (2013) Controlled synthesis and transfer of large-area WS<sub>2</sub> sheets: from single layer to few layers. *ACS Nano* 7(6):5235–5242
- [9] Ovchinnikov D, Allain A, Huang Y-S, Dumcenco D, Kis A (2014) Electrical transport properties of single-layer WS<sub>2</sub>. *ACS Nano* 8(8):8174–8181
- [10] Iqbal MW, Iqbal MZ, Khan MF, Shehzad MA, Seo Y, Park JH, Hwang C, Eom J (2015) High-mobility and air-stable single-layer WS<sub>2</sub> field-effect transistors sandwiched between chemical vapor deposition-grown hexagonal BN films. *Sci Rep* 5:10699
- [11] Guo H, Lan C, Zhou Z, Sun P, Wei D, Li C (2017) Transparent, flexible, and stretchable WS<sub>2</sub> based humidity sensors for electronic skin. *Nanoscale* 9(19):6246–6253
- [12] Lan C, Zhou Z, Zhou Z, Li C, Shu L, Shen L, Li D, Dong R, Yip S, Ho JC (2018) Wafer-scale synthesis of monolayer WS<sub>2</sub> for high-performance flexible photodetectors by enhanced chemical vapor deposition. *Nano Res* 11(6):3371–3384
- [13] Ratha S, Rout CS (2013) Supercapacitor electrodes based on layered tungsten disulfide-reduced graphene oxide hybrids synthesized by a facile hydrothermal method. *ACS Appl Mater Interfaces* 5(21):11427–11433
- [14] Godin K, Kang K, Fu S, Yang E-H (2016) Increased monolayer domain size and patterned growth of tungsten disulfide through controlling surface energy of substrates. *J Phys D* 49(32):325304
- [15] Walck S, Zabinski J, Donley M, Bultman J (1993) Evolution of surface topography in pulsed-laser-deposited thin films of MoS<sub>2</sub>. *Surf Coat Technol* 62(1–3):412–416
- [16] Bruncko J, Šutta P, Netřvalová M, Michalka M, Vincze A, Kovac J (2017) Comparative study of ZnO thin film prepared by pulsed laser deposition—comparison of influence of different ablative lasers. *Vacuum* 138:184–190
- [17] Fominski VY, Grigoriev S, Romanov R, Volosova M, Demin M (2015) Chemical composition, structure and light reflectance of W–Se and W–Se–C films prepared by pulsed laser deposition in rare and reactive buffer gases. *Vacuum* 119:19–29
- [18] Zhu B, Sun X, Zhao X, Su F, Li G, Wu X, Wu J, Wu R, Liu J (2008) The effects of substrate temperature on the structure and properties of ZnO films prepared by pulsed laser deposition. *Vacuum* 82(5):495–500
- [19] Debelo N, Dejene F, Roro K, Pricilla M, Oliphant C (2016) The effect of argon gas pressure on structural, morphological and photoluminescence properties of pulsed laser deposited KY<sub>3</sub>F<sub>10</sub>·Ho<sup>3+</sup> thin films. *Appl Phys A* 122(6):619
- [20] Dey PP, Khare A (2017) Stoichiometry-dependent linear and nonlinear optical properties of PLD SiO<sub>x</sub> thin films. *J Alloys Compd* 706:370–376
- [21] Yao J, Zheng Z, Shao J, Yang G (2015) Stable, highly-responsive and broadband photodetection based on large-area multilayered WS<sub>2</sub> films grown by pulsed-laser deposition. *Nanoscale* 7(36):14974–14981
- [22] Loh TA, Chua DH, Wee AT (2015) One-step synthesis of few-layer WS<sub>2</sub> by pulsed laser deposition. *Sci Rep* 5:18116
- [23] Loh TA, Chua DH (2015) Origin of hybrid 1T- and 2H-WS<sub>2</sub> ultrathin layers by pulsed laser deposition. *J Phys Chem C* 119(49):27496–27504
- [24] Yang Z, Hao J (2016) Progress in pulsed laser deposited two-dimensional layered materials for device applications. *J Mater Chem C* 4(38):8859–8878
- [25] Schenato M, Ricardo CLA, Scardi P, Edla R, Miotello A, Orlandi M, Morrish R (2016) Effect of annealing and nanostructuring on pulsed laser deposited WS<sub>2</sub> for HER catalysis. *Appl Catal A* 510:156–160
- [26] Torres-Torres C, Perea-López N, Elías AL, Gutiérrez HR, Cullen DA, Berkdemir A, López-Urías F, Terrones H, Terrones M (2016) Third order nonlinear optical response exhibited by mono-and few-layers of WS<sub>2</sub>. *2D Mater* 3(2):021005
- [27] Zheng X, Zhang Y, Chen R, Xu Z, Jiang T (2015) Z-scan measurement of the nonlinear refractive index of monolayer WS<sub>2</sub>. *Opt Exp* 23(12):15616–15623



- [28] Dey PP, Khare A (2017) Nonlinear optical and optical limiting response of PLD nc-Si thin films. *J Mater Chem C* 5(46):12211–12220
- [29] Liang G, Tao L, Tsang YH, Zeng L, Liu X, Li J, Qu J, Wen Q (2019) Optical limiting properties of a few-layer MoS<sub>2</sub>/PMMA composite under excitation of ultrafast laser pulses. *J Mater Chem C* 7(3):495–502
- [30] Chen T-H, Lin C-Y, Lin Y-H, Chi Y-C, Cheng C-H, Luo Z, Lin G-R (2016) MoS<sub>2</sub> nano-flake doped polyvinyl alcohol enabling polarized soliton mode-locking of a fiber laser. *J Mater Chem C* 4(40):9454–9459
- [31] Friberg S, Smith P (1987) Nonlinear optical glasses for ultrafast optical switches. *IEEE J Quantum Electron* 23(12):2089–2094
- [32] Weber M, Milam D, Smith W (1978) Nonlinear refractive index of glasses and crystals. *Opt Eng* 17(5):1754–63
- [33] Owyong A (1973) Ellipse rotation studies in laser host materials. *IEEE J Quantum Electron* 9(11):1064–1069
- [34] Sheik-Bahae M, Said AA, Van Stryland EW (1989) High-sensitivity, single-beam n<sub>2</sub> measurements. *Opt Lett* 14(17):955–957
- [35] Berkdemir A, Gutiérrez HR, Botello-Méndez AR, Perea-López N, Elías AL, Chia C-I, Wang B, Crespi VH, López-Urías F, Charlier J-C (2013) Identification of individual and few layers of WS<sub>2</sub> using Raman spectroscopy. *Sci Rep* 3:1755
- [36] Zhu Q, Chu X, Zhang Z, Dai W-L, Fan K (2013) A novel green process for the synthesis of glutaraldehyde by WS<sub>2</sub>@HMS material with aqueous H<sub>2</sub>O<sub>2</sub>. *RSC Adv* 3(6):1744–1747
- [37] Acsente T, Negrea RF, Nistor LC, Logofatu C, Matei E, Birjega R, Grisolia C, Dinescu G (2015) Synthesis of flower-like tungsten nanoparticles by magnetron sputtering combined with gas aggregation. *Eur Phys J D* 69(6):161
- [38] Lu M, Chien C (1990) Structural and magnetic properties of Fe–W alloys. *J Appl Phys* 67(9):5787–5789
- [39] Zheng D, Wu Y-p, Li Z-y, Cai Z-b (2017) Tribological properties of WS<sub>2</sub>/graphene nanocomposites as lubricating oil additives. *RSC Adv* 7(23):14060–14068
- [40] Zabinski J, Donley M, Prasad S, McDevitt N (1994) Synthesis and characterization of tungsten disulphide films grown by pulsed-laser deposition. *J Mater Sci* 29(18):4834–4839. <https://doi.org/10.1007/BF00356530>
- [41] Alfihed S, Hossain M, Alharbi A, Alyamani A, Alharbi FH (2013) PLD grown polycrystalline tungsten disulphide (WS<sub>2</sub>) films. *J Mater* 2013
- [42] Pradhan G, Sharma AK (2019) Temperature controlled 1T/2H phase ratio modulation in mono- and a few layered MoS<sub>2</sub> films. *Appl Surf Sci* 479:1236–1245
- [43] Liu Y, Xu G, Song C, Weng W, Du P, Han G (2007) Modification on Forouhi and Bloomer model for the optical properties of amorphous silicon thin films. *Thin Solid Films* 515(7–8):3910–3913
- [44] McGahan WA, Makovicka T, Hale J, Woollam JA (1994) Modified Forouhi and Bloomer dispersion model for the optical constants of amorphous hydrogenated carbon thin films. *Thin Solid Films* 253(1–2):57–61
- [45] Sundari ST (2005) Forouhi–Bloomer analysis to study amorphization in Si. *J Non-Cryst Solids* 351(52–54):3866–3869
- [46] Bayat A, Saievar-Iranizad E (2017) Synthesis of blue photoluminescent WS<sub>2</sub> quantum dots via ultrasonic cavitation. *J Lumin* 185:236–240
- [47] Yan Y, Zhang C, Gu W, Ding C, Li X, Xian Y (2016) Facile synthesis of water-soluble WS<sub>2</sub> quantum dots for turn-on fluorescent measurement of lipoic acid. *J Phys Chem C* 120(22):12170–12177
- [48] Ahn C, Lee J, Kim HU, Bark H, Jeon M, Ryu GH, Lee Z, Yeom GY, Kim K, Jung J (2015) Low-temperature synthesis of large-scale molybdenum disulfide thin films directly on a plastic substrate using plasma-enhanced chemical vapor deposition. *Adv Mater* 27(35):5223–5229
- [49] Kumar I, Khare A (2016) Optical nonlinearity in nanostructured carbon thin films fabricated by pulsed laser deposition technique. *Thin Solid Films* 611:56–61
- [50] Bharti GP, Khare A (2016) Structural and linear and nonlinear optical properties of Zn<sub>1-x</sub>Al<sub>x</sub>O (0 ≤ x ≤ 0.10) thin films fabricated via pulsed laser deposition technique. *Opt Mater Exp* 6(6):2063–2080
- [51] Kesarwani R, Khare A (2018) Surface plasmon resonance and nonlinear optical behavior of pulsed laser-deposited semitransparent nanostructured copper thin films. *Appl Phys B* 124(6):116
- [52] Dong N, Li Y, Zhang S, McEvoy N, Zhang X, Cui Y, Zhang L, Duesberg GS, Wang J (2016) Dispersion of nonlinear refractive index in layered WS<sub>2</sub> and WSe<sub>2</sub> semiconductor films induced by two-photon absorption. *Opt Lett* 41(17):3936–3939
- [53] Bayesteh S, Mortazavi SZ, Reyhani A (2018) Investigation on nonlinear optical properties of MoS<sub>2</sub> nanoflakes grown on silicon and quartz substrates. *J Phys D* 51(19):195302
- [54] Dey PP, Khare A (2016) Effect of substrate temperature on structural and linear and nonlinear optical properties of nanostructured PLD a-SiC thin films. *Mater Res Bull* 84:105–117
- [55] Rumaner L, Tazawa T, Ohuchi F (1994) Compositional change of (0001) WS<sub>2</sub> surfaces induced by ion beam bombardment with energies between 100 and 1500 eV. *J Vac Sci Technol* 12(4):2451–2456

- [56] Li D-H, Zheng H, Wang Z-Y, Zhang R-J, Zhang H, Zheng Y-X, Wang S-Y, Zhang DW, Chen L-Y (2017) Dielectric functions and critical points of crystalline WS<sub>2</sub> ultrathin films with tunable thickness. *Phys Chem Chem Phys* 19(19):12022–12031

**Publisher's Note** Springer Nature remains neutral with regard to jurisdictional claims in published maps and institutional affiliations.